mater.scichina.com link.springer.com

Published online 23 June 2021 | https://doi.org/10.1007/s40843-021-1683-0
Sci China Mater 2021, 64(12): 2976–2986

Defect tolerance in chalcogenide perovskite photovoltaic material $BaZrS_3$

Xiaowei Wu[1†], Weiwei Gao[2,3†], Jun Chai[1], Chen Ming[1*], Miaogen Chen[4], Hao Zeng[5], Peihong Zhang[5], Shengbai Zhang[6] and Yi-Yang Sun[1*]

ABSTRACT Chalcogenide perovskites (CPs) exhibiting lower band gaps than oxide perovskites and higher stability than halide perovskites are promising materials for photovoltaic and optoelectronic applications. For such applications, the absence of deep defect levels serving as recombination centers (dubbed defect tolerance) is a highly desirable property. Here, using density functional theory (DFT) calculations, we study the intrinsic defects in $BaZrS_3$, a representative CP material. We compare Hubbard-*U* and hybrid functional methods, both of which have been widely used in addressing the band gap problem of semi-local functionals in DFT. We find that tuning the *U* value to obtain experimental bulk band gap and then using the obtained *U* value for defect calculations may result in over-localization of defect states. In the hybrid functional calculation, the band gap of $BaZrS_3$ can be accurately obtained. We observe the formation of small S-atom clusters in both methods, which tend to self-passivate the defects from forming mid-gap levels. Even though in the hybrid functional calculations several relatively deep defects are observed, all of them exhibit too high formation energy to play a significant role if the materials are prepared under thermal equilibrium. $BaZrS_3$ is thus expected to exhibit sufficient defect tolerance promising for photovoltaic and optoelectronic applications.

Keywords: chalcogenide perovskite, photovoltaics, defect tolerance, $BaZrS_3$, first-principles calculation

INTRODUCTION

In the past decade, perovskite materials have been successfully used as semiconductors for photovoltaic [1–8], photodetection [9–13] and light-emitting applications [14–20]. This is different from the traditional uses of perovskites mainly for dielectric applications, such as piezoelectrics and ferroelectrics [21,22]. The semiconducting perovskite materials intensively studied in recent years are dominated by halides [1–20]. The low conduction band due to strong spin-orbit coupling in cations such as lead and the high valence band due to the anions such as iodine 6p orbitals synergically reduce the band gap of the halide perovskites to a region suited for photovoltaic devices [23]. Other interesting physics such as defect tolerance allows the materials to be readily prepared for device fabrication with less need for high purity and high crystallinity while maintaining the low production cost. Currently, two main barriers for the halide perovskites to be deployed in larger scale are the stability issue partly caused by the organic components and the toxicity mainly due to the use of lead [24,25].

Chalcogenide perovskites (CPs) were first synthesized in 1957 [26]. Since then, while a number of CPs have been reported, their physical properties have only been studied sporadically [27–29]. Inspired by the success of halide perovskites, CPs have been proposed for photovoltaic applications [30–32]. The optical properties of II-IV-S_3 CPs have been studied experimentally [31,33,34]. These CPs are air stable and contain only non-toxic elements. Among them, $BaZrS_3$ having a band gap of about 1.8 eV [31,33–35] is suited for making solar cells, in particular,

[1] State Key Laboratory of High Performance Ceramics and Superfine Microstructure, Shanghai Institute of Ceramics, Chinese Academy of Sciences, Shanghai 201899, China
[2] School of Physics, Dalian University Technology, Dalian 116024, China
[3] Center for Computational Materials, Oden Institute for Computational Engineering and Sciences, The University of Texas at Austin, Austin, TX 78712, United States
[4] College of Science, China Jiliang University, Hangzhou 310018, China
[5] Department of Physics, University at Buffalo, The State University of New York, Buffalo, NY 14260, United States
[6] Department of Physics, Applied Physics & Astronomy, Rensselaer Polytechnic Institute, Troy, NY 12180, United States
† These authors contributed equally to this work.
* Corresponding authors (emails: yysun@mail.sic.ac.cn (Sun YY); mingchen@mail.sic.ac.cn (Ming C))

© Science China Press and Springer-Verlag GmbH Germany, part of Springer Nature 2021

when combined with silicon-based solar cells for two-junction tandem solar cells. Ti-doping has been attempted to optimize solar light absorption by reducing the band gap [31,36]. Thin films of $BaZrS_3$ have also been prepared with their electronic and optical properties being reported [37–40]. Encouragingly, $SrHfS_3$ has been experimentally demonstrated to exhibit excellent green light-emitting properties [41]. Recently, we found that III-III-S_3 CPs could possess wider band gaps than II-IV-S_3 CPs and hold promise for broader applications such as transparent conducting materials [42].

With the attractive application potentials, it is of great interest to understand the defect properties of CPs because defect tolerance has been considered as one of the unique properties of halide perovskites [43–50]. For photovoltaic and optoelectronic materials, recombination centers (RCs) are the defects to be avoided as they compete with the desired functions of carriers, i.e., producing current or light. It has been shown that intrinsic defects in halide perovskites are mostly shallow defects, which do not serve as effective RCs [43]. Such a property allows low-cost synthesis of the materials and low-cost fabrication of the devices without demanding control on structural defects.

The defect properties of $BaZrS_3$ were studied by density functional theory (DFT), where Hubbard U of 4.5 eV was applied to Zr 4d orbitals to obtain the experimental band gap [31]. Usually, 4d transition metals (TMs) have much delocalized d orbitals than 3d TMs. While using U values of about 4.5 eV may be appropriate for the 3d TMs, they are too large for 4d TMs. Large U values could result in over-localized d orbitals and in turn affect the defect properties. Regarding the band gap problem in DFT, the hybrid functional of Heyd, Scuseria and Ernzerhof (HSE) by partly incorporating Hartree-Fock exchange is particularly useful for the CPs. The predicted band gaps using the HSE functional are in good agreement with experiments without tuning the empirical parameters of HSE. It is therefore desirable to study the defect properties using the HSE functional.

In this paper, we report a comparative study on the defect properties of $BaZrS_3$ using different functionals. We start from the semi-local PBEsol functional. Then, by systematically tuning the U value for Zr 4d we illustrate the effect of Hubbard U on the defect properties. It is found that the defect level could undergo a sudden transition from shallow to deep when U is above a threshold. We then carry out the first-principles calculation on the U value of Zr 4d in $BaZrS_3$ and show that the U value is as small as 1.1 eV and produces shallow defect levels only. Finally, to achieve more conclusive results on the defect properties of $BaZrS_3$, we calculate the defect transition levels and defect formation energies using the HSE functional. While several defects with relatively deep levels have been identified, their high formation energy suggests that they can be avoided under thermal equilibrium. Together, these results show that $BaZrS_3$ is substantial defect-tolerant for photovoltaic and optoelectronic applications.

COMPUTATIANAL METHODS

DFT calculations were carried out using Vienna *ab initio* simulation (VASP) package [51,52], which describes the interaction between the ion-cores and valence electrons by projector augmented wave (PAW) potentials [53]. Plane waves with cutoff energy of 20 Ry were taken as a basis set. Different exchange-correlation functionals were adopted, namely, PBEsol [54], PBEsol+U [55] and HSE [56]. The supercell method was used to model the defects. A 160-atom supercell was constructed from the 20-atom unit cell by a conversion matrix of (2 0 0; 0 1 −1; 0 2 2). The Γ point was used to represent the Brillouin zone. Calculations were spin-polarized if a defect possesses a spin magnetic moment. The atomic structures were fully relaxed until the calculated forces on all atoms were less than 1 mRy $Bohr^{-1}$. The lattice constants were optimized by using each functional with increased cutoff energy of 30 Ry and compared with experimental results in Table 1. A 3 × 2 × 3 Monkhorst-Pack k-point grid was used in the bulk calculations.

The formation energy of a point defect carrying a charge q was calculated following [58,59]:

$$\Delta H(\{\mu_i\}, E_F, q) = E_D(q) - E_0 + \sum_i n_i(E_i + \mu_i) + q(E_{VBM} + E_F),$$

where $E_D(q)$ is the total energy of the supercell containing a point defect of charge q, E_0 is the total energy of the perfect supercell, n_i is the number of atoms which are added (n_i < 0) or removed (n_i > 0) from the supercell during the formation of the defects, μ_i is the chemical

Table 1 Lattice constants of $BaZrS_3$ optimized by different functionals and used in defect calculations. In the PBEsol+U calculation, the U value is determined from first-principles calculation as described in the text. Experimental results [57] are also listed for comparison.

Functional	a (Å)	b (Å)	c (Å)
PBEsol	7.118	9.932	6.953
PBEsol+U	7.121	9.961	6.976
HSE	7.148	10.020	7.024
Experimental	7.060	9.981	7.025

 © Science China Press and Springer-Verlag GmbH Germany, part of Springer Nature 2021

potential of the constituent element i referenced to the total energy per atom of element i in its stable phase (E_i), E_F is the Fermi energy referenced to the valence band maximum (VBM) of the host material (E_{VBM}). The allowed range for μ_i is determined by the existence of various secondary phases, which will be described in more details below. The Fermi energy E_F generally varies between E_{VBM} and the conduction band minimum (CBM) of the host material. The defect transition level, at which the thermodynamically stable charge state of the defect switches from q to q', is given by $\varepsilon(q/q') = [E_D(q) - E_D(q')]/(q' - q) - E_{VBM}$, which indicates whether the defect is deep or shallow.

First-principles calculation on the Hubbard U and J parameters were conducted with the constrained random phase approximation (cRPA) [60]. The details of our code implementation are presented in Refs. [61,62]. Here we briefly review the main steps. We first perform DFT calculations with planewave-based pseudopotential code PARATEC [63] to prepare a set of frontier Kohn-Sham states and projections of Zr d orbitals on these states. Using Zr 4d orbitals as the initial guesses, we construct maximally localized Wannier functions using Wannier90 code [64]. Next, we use BerkeleyGW code [65] to calculate cRPA screened Coulomb potential W^{cRPA}. Then, the interaction matrix elements $<ij|W^{cRPA}|ij>$ and $<ij|W^{cRPA}|ji>$ are computed, where i, j are Wannier function indices. Finally, the Hubbard U and J parameters are obtained by $U = 1/25\sum_{ij}<ij|W^{cRPA}|ij>$ and $J = 1/20\sum_{i\neq j}<ij|W^{cRPA}|ji>$, respectively. Note that in defect calculations by VASP, we set the effective U value to be the difference between the U and J values (i.e., $U - J$) obtained from the cRPA calculation.

RESULTS AND DISCUSSION

RCs and carrier traps

Before discussing the results, we first explain the RCs to be studied in this work. Fig. 1 shows the two types of RCs through a Shockley-Read-Hall (SRH) process. The type I RC starts from a neutral defect. In step 1, it captures an electron and becomes a negative center. In step 2, the negative center will scatter electrons, but capture a hole. In step 3, the captured electron and hole recombine and accomplish an SRH process. The type I RC could also capture a hole first in step 1, and then capture an electron in step 2.

The type II RC starts from a charged defect. While Fig. 1 shows the negatively charged case, starting from a positively charged defect can be treated similarly. For type II RC, in step 2, the negative center captures a hole first and in step 3 it captures an electron. Then, the step 3 will be the same as that in type I RC. Even though in step 2, the neutral center has a similar chance of capturing a hole, this process cannot accomplish an SRH process. Therefore, as long as one hole is re-emitted (the short black wavy arrow in Fig. 1), it will be able to capture an electron.

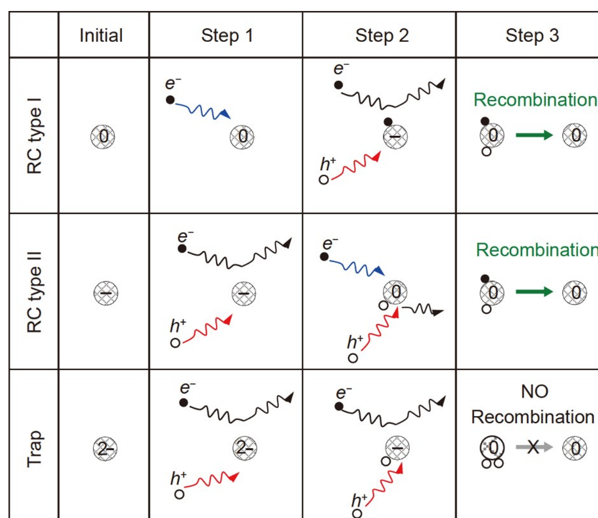

Figure 1 Schematic showing the difference between RCs and carrier traps. See text for detailed discussion.

It is necessary to differentiate the RCs from carrier traps. Fig. 1 illustrates the case for a defect carrying 2− charge. The discussion below applies to charges higher than 1 regardless of the charge types. In the case of 2− charge, the defect will capture a hole in step 1. Then, in step 2, because it is still a negative center, it cannot capture an electron to accomplish an SRH process. Instead, it will capture another hole. Thus, in step 3 no recombination could occur.

Based on the discussions above, we know that only the $\varepsilon(0/-)$ and $\varepsilon(+/0)$ levels are responsible for the SRH recombination. For this reason, we will only discuss the $\varepsilon(0/-)$ and $\varepsilon(+/0)$ levels below. This provides another advantage: for singly charged defects, the error due to image charge interaction under the periodic boundary condition can be neglected. For our case, with a supercell size of about 15.9 Å and a calculated relative dielectric constant of 12, we estimate the error to be smaller than 0.1 eV using the Madelung correction [66].

Effect of Hubbard U on defect properties

We considered 12 possible intrinsic point defects, namely, vacancies (V_{Ba}, V_{Zr}, V_S), interstitials (Ba_i, Zr_i, S_i) and anti-

 © Science China Press and Springer-Verlag GmbH Germany, part of Springer Nature 2021

site substitutions (Ba_{Zr}, Zr_{Ba}, Ba_S, S_{Ba}, Zr_S, S_{Zr}). We first show the results from semi-local PBEsol functional. Fig. 2a shows the calculated transition levels. It is seen that all defects have transition levels around band edges or outside the band gap. V_{Ba} and Ba_{Zr} are shallow acceptors, while V_S, Ba_i, Zr_i, Zr_{Ba}, Ba_S and Zr_S are shallow donors. V_{Zr}, S_i, S_{Ba} and S_{Zr} behave as fully self-passivated defects with their donor levels near the VBM and acceptor levels above the CBM. We will further discuss the defect behaviors in detail below.

The issue with the PBEsol functional is the well-known band-gap problem, which results in a severely underestimated band gap of 0.86 eV. The Hubbard U (i.e., the on-site Coulombic interaction) could partly compensate for the self-interaction error of the semi-local functionals and correct the over-delocalization of the local orbitals. A side effect of the Hubbard U is the opening of the band gap of semiconductors. This has been widely used to address the band gap problem of DFT in defect studies.

Meng *et al.* [31] investigated the defect transition levels of $BaZrS_3$ using PBE+U method. The value of U was set to be 4.5 eV, which yielded a band gap of 1.72 eV, consistent with experimental results. In this study, several defects have been reported to be deep-level defects, including S_i, S_{Zr}, S_{Ba}, Zr_i and Zr_S. In particular, S_{Zr} exhibits a deep $\varepsilon(0/-)$ transition level at about 0.4 eV above the VBM. This result contradicts the PBEsol results as shown in Fig. 2a. Taking this defect as an example, we carried out a U-dependent defect study to understand the reason for the deep transition level found in the PBE+U calculation.

Fig. 3a shows the variations of the band gap and the $\varepsilon(0/-)$ level of S_{Zr} as a function of U. For each U value from 0 to 4.5 eV, we re-optimized the defect structures at both the neutral and 1− charge states. Totally 11 U values were considered. It can be seen that the band gap linearly increases with the increase of U. Interestingly, the $\varepsilon(0/-)$ level undergoes a sharp transition from being inside the conduction band to being in the middle of the band gap. The transition occurs at a U value between 2.6 and 2.7 eV. Fig. 3b shows a schematic of the Kohn-Sham levels at U = 2.6 and 2.7 eV near the band edges. When U = 2.6 eV, there is an electron occupying the CBM and the defect is fully delocalized as shown in Fig. 3c. As a result, no local spin magnetic moment is associated with the defect. In contrast, when U = 2.7 eV, a mid-gap state appears, which is spin-polarized with the electron occupying the spin-up orbital. The corresponding mid-gap state is shown in Fig. 3d, which is localized around the defect. Clearly, the localization of electronic state induced by large U value results in the deep $\varepsilon(0/-)$ transition level.

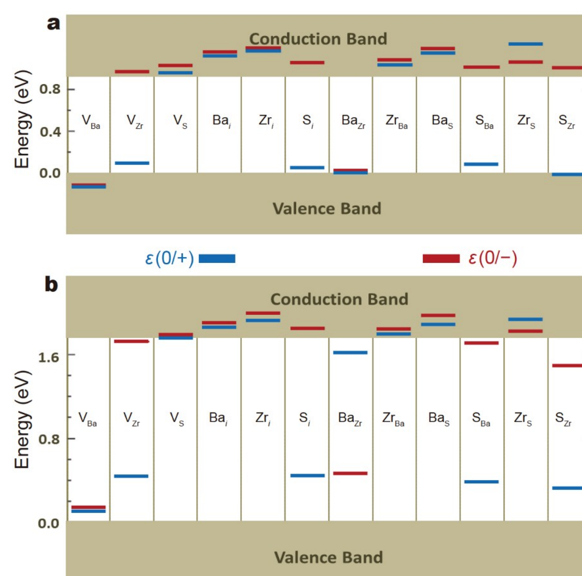

Figure 2 Defect transition levels in $BaZrS_3$ calculated by (a) PBEsol and (b) HSE functionals.

Determination of U value in $BaZrS_3$

In order to determine the U value of Zr 4d orbitals in $BaZrS_3$, we carried out cRPA calculations based on the method described in the COMPUTATIANAL METHODS section. $BaZrS_3$ has a 20-atom unit cell containing 4 Zr atoms and 12 S atoms with totally 20 Zr 4d orbitals and 36 S 3p orbitals, which dominate the band edge states [33]. Therefore, we constructed 56 Wannier functions using 76 Kohn-Sham orbitals covering the energy window from −5 to 5 eV. For the construction of Wannier functions and cRPA calculations, we used a 4 × 3 × 4 Monkhorst-Pack k-grid, a 80 Ry cutoff for wave functions, and a 30 Ry cutoff for dielectric matrix.

In Fig. 4a, we can see that the constructed Wannier functions display Zr 4d features. Two of them resemble e_g orbitals and the other three resemble t_{2g} orbitals. The comparison in Fig. 4b shows that the band structure interpolated with our Wannier functions well matches the band structure calculated directly with DFT. Our calculated U and J matrix elements are shown in Fig. 4c. The average of the U matrix elements is 1.37 eV and the average of the J matrix elements is 0.24 eV. These values are significantly smaller than those of 3d or 4d late TM elements since Zr 4d orbitals are more spatially extended. In Fig. 4d, we compare the radial parts of atomic wave functions of Zr 4d orbitals with those of Cu 3d, Ag 4d, and S 3p orbitals. Clearly, the radial atomic wave functions of Zr 4d electrons are more extended than those of Cu 3d and Ag 4d electrons, but similar to those of S 3p

 © Science China Press and Springer-Verlag GmbH Germany, part of Springer Nature 2021

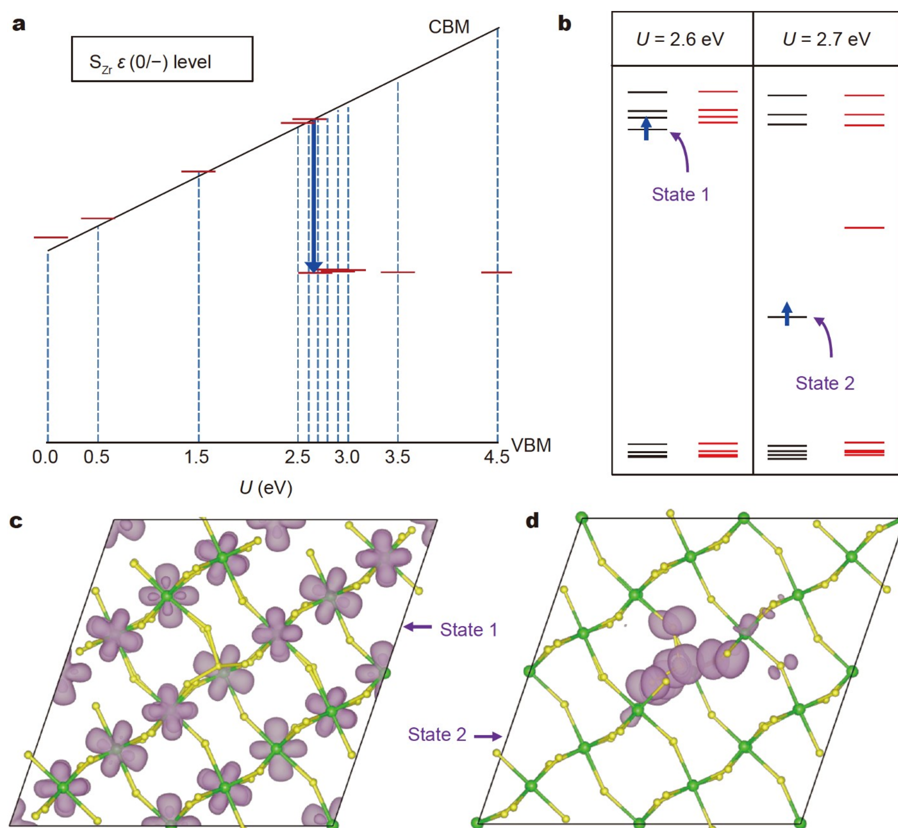

Figure 3 (a) Transition level $\varepsilon(0/-)$ of S_{Zr} as a function of U value for Zr 4d orbital. (b) Schematic of eigenvalues near the band edges at Γ point of the supercell containing the S_{Zr} defect in 1− charge state calculated using U = 2.6 and 2.7 eV. (c, d) The charge density plots of the states 1 and 2 marked in (b).

electrons. This comparison suggests that Zr 4d should have a smaller U value than those of the d electrons of late TM elements. In an alternative approach, we also calculated matrix elements $U_{ij}' = \langle d_i d_j | W^{cRPA} | d_i d_j \rangle$ and $J_{ij}' = \langle d_i d_j | W^{cRPA} | d_j d_i \rangle$, where the Wannier functions are replaced with d_i and d_j, the pseudo-atomic wave functions of Zr 4d orbitals. We find U' = 1.4 eV and J' = 0.3 eV, which are close to what we find using Wannier functions and further validate our results above.

With the U = 1.37 eV and J = 0.24 eV as determined above, we recalculated the defect transition levels based on the PBEsol functional. Compared with the results in Fig. 2a, the PBEsol+U calculations yield qualitatively the same results as those from the PBEsol calculations even though the band gap is increased from 0.86 to 1.00 eV. All defects show shallow transition levels to within 0.1 eV from the band edges (Fig. S1).

Effect of Hartree-Fock exchange

The band gap from the PBEsol+U calculation is still about 0.8 eV smaller than the experimental results. The HSE functional is known to accurately predict the band gaps for CPs [67]. We calculated the defect transition levels using the HSE functional. For easy comparison with the PBEsol results, we show the results in Fig. 2b. The behaviors of these defects are discussed below.

Among the three vacancy defects, V_{Ba} and V_S are a shallow acceptor and a shallow donor, respectively. Generally, a cation vacancy forms an acceptor, while an anion vacancy forms a donor. The Ba and S vacancies follow this rule. V_{Zr} is more complicated than the other two vacancies. It is expected to be an acceptor defect similar to V_{Ba}. However, around the Zr vacancy there are six S atoms which exhibit "dangling" bonds if viewed from a covalent-bonding picture. Our calculations show that one of the S atoms deviates from its original position and moves towards two opposite S atoms and form an S–S–S bridged trimer structure, as illustrated in Fig. 5a. As a result, the V_{Zr} defect unexpectedly behaves as a deep donor with the $\varepsilon(0/+)$ transition level located at about

 © Science China Press and Springer-Verlag GmbH Germany, part of Springer Nature 2021

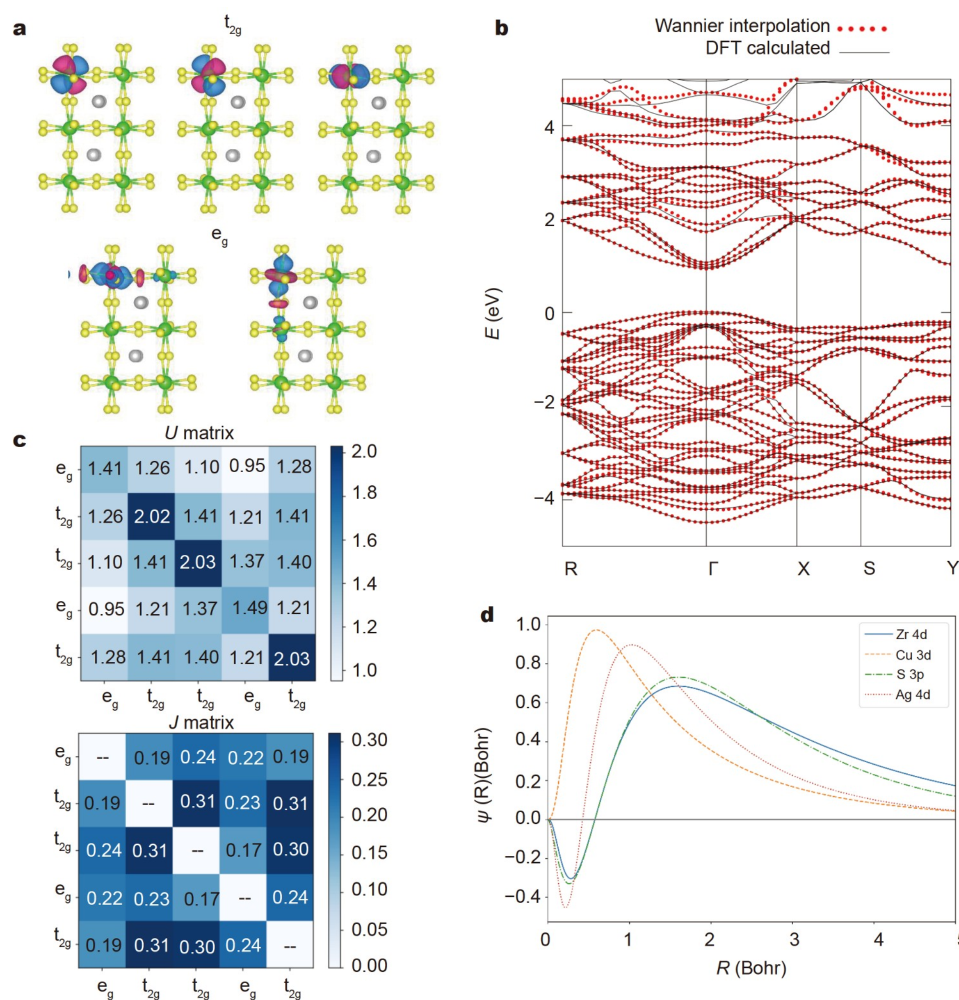

Figure 4 (a) Isosurfaces of maximally localized Wannier functions, which resemble Zr 4d's t_{2g} and e_g orbitals under an octahedral crystal field. (b) Comparison between the band structure calculated with DFT and that interpolated with Wannier functions. (c) Calculated elements of *U* and *J* matrices using the cRPA method. (d) Radial part of atomic wave functions of different elements calculated.

1.35 eV below the CBM. The structure without forming the S trimer is metastable and it is higher in energy than the S-trimer structure by 3.36 eV in the neutral state. This structure is an acceptor, as expected, with the $\varepsilon(0/-)$ transition level 0.17 eV above the VBM.

Among the three interstitial defects, Ba_i and Zr_i are shallow donors. S_i is expected to be an acceptor. However, an S-dimer forms as shown in Fig. 5b. As a result, S_i behaves as a deep donor with the $\varepsilon(0/+)$ transition level located at about 1.33 eV below the CBM. The S-dimer serves as a 2− anion, i.e., $(S_2)^{2-}$, similar to the S^{2-} anion. Such kind of anion dimers are also referred to as split-interstitial defects. In some bulk sulfides, e.g., pyrite FeS_2, the $(S_2)^{2-}$ anions can also be found.

Among the six anti-site defects, Ba_{Zr}, S_{Ba} and S_{Zr} are expected to be acceptors, while Zr_{Ba}, Ba_S and Zr_S are expected to be donors. However, the behaviors of the S_{Ba} and S_{Zr} defects are not as expected. They behave as donors instead. Again, it is because of the formation of extra S–S bonds. In the case of S_{Ba}, an S–S–S bridge structure forms (see Fig. 5c) similar to the case of V_{Zr}, while in the case of S_{Zr} an S-tetramer forms (see Fig. 5d).

Overall, among all the intrinsic defects, V_{Ba} is the only relatively shallow acceptor with $\varepsilon(0/-)$ 0.14 eV above the VBM, while V_S, Ba_i, Zr_i, Zr_{Ba}, Ba_S and Zr_S are all shallow donors. We also checked higher charge states of these shallow defects (see Fig. S2) and confirmed their shallow nature, namely, the transition levels for the higher charge states are also at the VBM (for V_{Ba}) or CBM (for the shallow donors). We will not discuss the atomic and

 © Science China Press and Springer-Verlag GmbH Germany, part of Springer Nature 2021

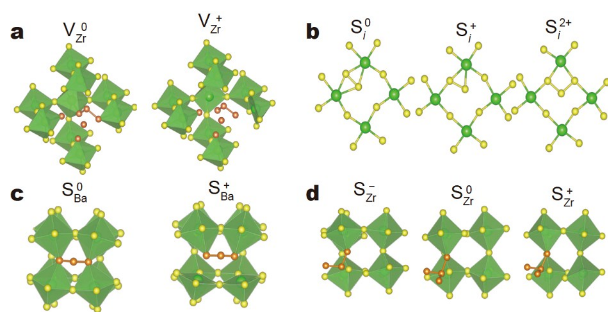

Figure 5 Atomic structures of four deep donor defects (a) V_{Zr}, (b) S_i, (c) S_{Ba}, and (d) S_{Zr} at different charge states. In (a, c, d), the S trimer and tetramers are highlighted by a dark color.

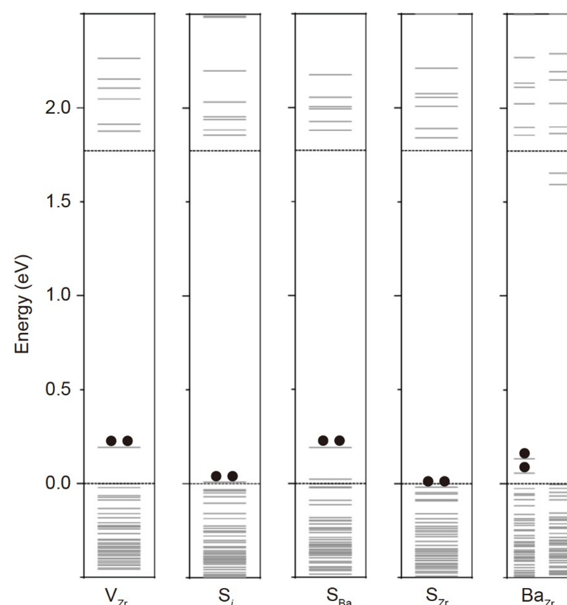

Figure 6 Eigenvalue spectra of five defects at Γ point of the supercell. All defects are in neutral charge state. The dashed lines mark the band gap. The energy zero is aligned to the bulk VBM. The highest occupied states are marked by two dots for the four non-spin-polarized defects. For Ba_{Zr}, which is spin-polarized, the two spin-up gap states are marked by a single dot.

electronic structures of these shallow donor defects in detail below.

Among the four deep donor defects, namely, V_{Zr}, S_i, S_{Ba} and S_{Zr}, the formation of the S clusters (dimer, trimer and tetramer) tends to remove mid-gap states in the neutral charge state and leaves behind a relatively clean band gap. The Γ-point eigenvalue spectra of the four defects in the neutral charge state are shown in Fig. 6, where it can be seen that the S_i and S_{Zr} defects show no gap defect states in the band gap. The removal of deep "dangling bond" states by self-passivation is desired for a semiconductor being defect-tolerant. For this type of defects, usually the acceptor levels are as deep as close to the CBM and the donor levels are as deep as close to the VBM if the atomic structures of the charged states do not deviate from the neutral ones significantly. Unfortunately, structural relaxation in the 1+ state of V_{Zr}, S_i, S_{Ba} and S_{Zr} leads to the deep donor levels seen in Fig. 2b.

Taking the S_i defect as an example, in the 1+ state it undergoes a structural change, as shown in Fig. 5b, where it can be seen that one of the S–Zr bonds is broken. If further charging the defect to 2+, another S–Zr bond will be broken and the defect structure looks more like a typical interstitial defect, also shown in Fig. 5b. For the other three defects, similar S–Zr bond breaking (or weakening) in the 1+ charge state results in the deep donor levels shown in Fig. 5. Moreover, the S_{Zr} defect in the 1− charge state also undergoes a structural relaxation which stabilizes this charge state so that the S_{Zr} defect could also be a deep acceptor, as shown in Fig. 5d. However, the $\varepsilon(0/-)$ transition level is much closer to the CBM compared with the PBE+U calculation using U = 4.5 eV, which results in $\varepsilon(0/-)$ close to the VBM.

In Hartree-Fock-based hybrid functional calculations, we previously found that even in a perfect supercell, adding or removing an electron from the system will give rise to mid-gap electronic states without creating any atomic defect [68]. By cutting the long-range part of exchange interaction, the HSE functional can mitigate this problem. To confirm these deep donor defects, we employed a 320-atom supercell to calculate the V_{Zr}, S_i, and S_{Ba} defects and found that the $\varepsilon(0/+)$ levels are 1.28, 1.34 and 1.40 eV, respectively, below the CBM, which differ from the results using the 160-atom supercell by 0.07, 0.01 and 0.01 eV, respectively, suggesting the accuracy using the 160-atom supercell.

Finally, we discuss the Ba_{Zr} defect. Our calculation shows that it is an amphoteric defect with its neutral charge state being unstable regardless of the position of the Fermi level. While being a deep acceptor, Ba_{Zr} is also a shallow donor. Compared with the case of V_{Zr}, the presence of an extra Ba atom hinders the formation of an S-trimer. Without forming the S-trimer, its neutral state exhibits unpaired electrons, as shown in Fig. 6, with magnetic moment of 2 μ_B. As mentioned above, the V_{Zr} defect without forming the S-trimer is already a relatively deep acceptor. Here, the acceptor level of Ba_{Zr} is even deeper (0.46 eV above the VBM) partly because of the presence of Ba cation which could stabilize the captured electron by Coulombic interaction. However, if positively charged, an S-dimer will form with an S–S distance of

 © Science China Press and Springer-Verlag GmbH Germany, part of Springer Nature 2021

2.06 Å giving rise to a relatively shallow donor level of 0.14 eV below the CBM. Again, the flexibility of S anions forming the S-clusters significantly influences the behavior of Ba_{Zr} similar to the other deep-level defects discussed above. However, different from the deep defect discussed above, its lowest unoccupied state contains significant contribution from the S 3p orbitals, which are hybridized with the Zr 4d states (see Fig. S3). For the other deep defects, their lowest unoccupied states are pure Zr 4d orbitals (see Fig. S4). The highest occupied state of the Ba_{Zr} defect is a localized state mainly contributed by S 3p orbitals.

Defect formation energy

We next calculated the defect formation energies of the intrinsic defects using the HSE functional. We first determined the allowed region for the chemical potentials that enables the formation of the primary phase of $BaZrS_3$ while avoiding possible secondary phases. We considered the two secondary phases, BaS in the rock-salt structure and ZrS_2 in the 1T structure. The calculated enthalpy of formation of BaS and ZrS_2 with respect to the constituent elements are −4.53 and −5.08 eV per formula unit, respectively. The elements were calculated using the body-centered cubic Ba, hexagonal close-packed Zr and S in the α-phase. The formation energy of $BaZrS_3$ with respect to BaS and ZrS_2 is thus −0.33 eV per formula unit. As shown in Fig. 7a, the allowed region for the chemical potentials is bounded by the D, E, F, and G points. The values of the chemical potentials at these points are listed in Fig. 7a.

The calculated defect formation energies in the neutral charge state are shown in Fig. 7b. Interestingly, the deep-level defects, i.e., Ba_{Zr}, V_{Zr}, S_i, S_{Ba} and S_{Zr}, all have rather high formation energies as long as the chemical potential moves slightly away from the D and F points, which corresponds to S-rich conditions. The low-energy defects with formation energies less than 1 eV are V_S, Zr_i, Zr_{Ba} and Zr_S, which are all shallow donors. The only shallow acceptor V_{Ba} has a formation energy of at least 3.6 eV. Therefore, we conclude that $BaZrS_3$ cannot be intrinsically p-type. This is different from previous conclusion using PBE+U calculation, which suggests that the material can be grown p-type if the growth condition is controlled under S-rich condition [31]. Fig. 7b shows that V_S is the dominant defect that governs the conduction type of the material, which is consistent with our recent

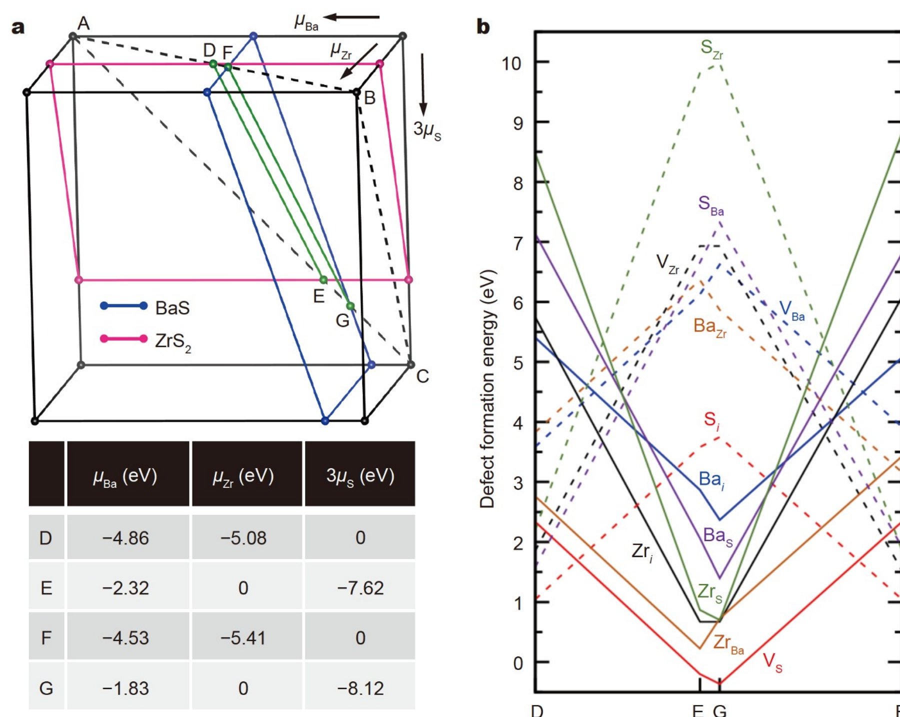

	μ_{Ba} (eV)	μ_{Zr} (eV)	$3\mu_S$ (eV)
D	−4.86	−5.08	0
E	−2.32	0	−7.62
F	−4.53	−5.41	0
G	−1.83	0	−8.12

Figure 7 (a) Determination of chemical potentials for calculating defect formation energies in $BaZrS_3$. The triangle ABC is determined by $\mu_{Ba} + \mu_{Zr} + 3\mu_S = \Delta H(BaZrS_3) = -9.94$ eV. The allowed region DEGF is determined by the relations $\mu_{Ba} + \mu_S \le \Delta H(BaS) = -4.53$ eV and $\mu_{Zr} + 2\mu_S \le \Delta H(ZrS_2) = -5.08$ eV. The lower panel of (a) shows the chemical potentials of (μ_{Ba}, μ_{Zr}, $3\mu_S$) at the D, E, F and G points. (b) Defect formation energies of 12 intrinsic defects in $BaZrS_3$ at the D, E, G and F points calculated by the HSE functional in the neutral state.

 © Science China Press and Springer-Verlag GmbH Germany, part of Springer Nature 2021

experiment on $BaZrS_3$ thin films [37]. Our results also suggest that Zr as a TM element is reactive enough to form sufficient bonding with neighboring S atoms to lower its formation energy when inserted into the lattice as an interstitial. In particular, the Zr_{Ba} antisite defect is the second lowest in formation energy over a large region of chemical potentials, which also happens to be a shallow donor. Under S-rich condition, S_i defect may form if the synthesis temperature is sufficiently high and the annealing process is not sufficiently long.

CONCLUSIONS

We carried out a comparative study on the intrinsic defects of CP $BaZrS_3$ using different DFT functionals and considering both the Hubbard U effect and the Hartree-Fock exchange. We show that tunning band gap towards the experimental value requires unphysically large U value, which in turn results in over-localization of the electronic states and deep defect levels. Using U and J values of 1.37 and 0.24 eV, respectively, determined from first-principles calculation, we found that the intrinsic defects of $BaZrS_3$ are all shallow-level defects, similar to the results obtained from the PBEsol functional, where V_{Ba} and Ba_{Zr} are shallow acceptors, V_S, Ba_i, Zr_i, Zr_{Ba}, Ba_S and Zr_S are shallow donors, and V_{Zr}, S_i, S_{Ba} and S_{Zr} behave as self-passivated defects (i.e., without "dangling bond" mid-gap states) in the neutral charge state. The self-passivation behavior is achieved by the formation of small S clusters and is highly desirable for a semiconductor being defect-tolerant. In HSE calculations, V_{Zr}, S_i, S_{Ba} and S_{Zr} show deep donor levels emerging from the VBM, suggesting that the self-passivation is not thorough. Nevertheless, all the deep-level defects from HSE, including Ba_{Zr}, show high formation energies, especially when the experimental condition is not extremely S-rich. With these results, we conclude that $BaZrS_3$ is sufficiently defect-tolerant, which is desirable for photovoltaic and optoelectronic applications.

Received 26 February 2021; accepted 8 April 2021; published online 23 June 2021

1 Kojima A, Teshima K, Shirai Y, *et al.* Organometal halide perovskites as visible-light sensitizers for photovoltaic cells. J Am Chem Soc, 2009, 131: 6050–6051
2 Lee MM, Teuscher J, Miyasaka T, *et al.* Efficient hybrid solar cells based on meso-superstructured organometal halide perovskites. Science, 2012, 338: 643–647
3 Burschka J, Pellet N, Moon SJ, *et al.* Sequential deposition as a route to high-performance perovskite-sensitized solar cells. Nature, 2013, 499: 316–319
4 Liu M, Johnston MB, Snaith HJ. Efficient planar heterojunction perovskite solar cells by vapour deposition. Nature, 2013, 501: 395–398
5 Green MA, Ho-Baillie A, Snaith HJ. The emergence of perovskite solar cells. Nat Photon, 2014, 8: 506–514
6 Jeon NJ, Noh JH, Yang WS, *et al.* Compositional engineering of perovskite materials for high-performance solar cells. Nature, 2015, 517: 476–480
7 Saliba M, Matsui T, Domanski K, *et al.* Incorporation of rubidium cations into perovskite solar cells improves photovoltaic performance. Science, 2016, 354: 206–209
8 McMeekin DP, Sadoughi G, Rehman W, *et al.* A mixed-cation lead mixed-halide perovskite absorber for tandem solar cells. Science, 2016, 351: 151–155
9 Fang Y, Dong Q, Shao Y, *et al.* Highly narrowband perovskite single-crystal photodetectors enabled by surface-charge recombination. Nat Photon, 2015, 9: 679–686
10 Büchele P, Richter M, Tedde SF, *et al.* X-ray imaging with scintillator-sensitized hybrid organic photodetectors. Nat Photon, 2015, 9: 843–848
11 Tan Z, Wu Y, Hong H, *et al.* Two-dimensional $(C_4H_9NH_3)_2PbBr_4$ perovskite crystals for high-performance photodetector. J Am Chem Soc, 2016, 138: 16612–16615
12 Kim YC, Kim KH, Son DY, *et al.* Printable organometallic perovskite enables large-area, low-dose X-ray imaging. Nature, 2017, 550: 87–91
13 Chen Q, Wu J, Ou X, *et al.* All-inorganic perovskite nanocrystal scintillators. Nature, 2018, 561: 88–93
14 Tan ZK, Moghaddam RS, Lai ML, *et al.* Bright light-emitting diodes based on organometal halide perovskite. Nat Nanotech, 2014, 9: 687–692
15 Stranks SD, Snaith HJ. Metal-halide perovskites for photovoltaic and light-emitting devices. Nat Nanotech, 2015, 10: 391–402
16 Cho H, Jeong SH, Park MH, *et al.* Overcoming the electroluminescence efficiency limitations of perovskite light-emitting diodes. Science, 2015, 350: 1222–1225
17 Swarnkar A, Marshall AR, Sanehira EM, *et al.* Quantum dot-induced phase stabilization of α-$CsPbI_3$ perovskite for high-efficiency photovoltaics. Science, 2016, 354: 92–95
18 Zhang L, Yang X, Jiang Q, *et al.* Ultra-bright and highly efficient inorganic based perovskite light-emitting diodes. Nat Commun, 2017, 8: 15640
19 Xiao Z, Kerner RA, Zhao L, *et al.* Efficient perovskite light-emitting diodes featuring nanometre-sized crystallites. Nat Photon, 2017, 11: 108–115
20 Lin K, Xing J, Quan LN, *et al.* Perovskite light-emitting diodes with external quantum efficiency exceeding 20 percent. Nature, 2018, 562: 245–248
21 Jaffe W, Cook WR, Jaffe H. Piezoelectric Ceramics. London: Academic Press, 1971
22 Zhang S, Li F, Jiang X, *et al.* Advantages and challenges of relaxor-$PbTiO_3$ ferroelectric crystals for electroacoustic transducers—A review. Prog Mater Sci, 2015, 68: 1–66
23 Amat A, Mosconi E, Ronca E, *et al.* Cation-induced band-gap tuning in organohalide perovskites: Interplay of spin-orbit coupling and octahedra tilting. Nano Lett, 2014, 14: 3608–3616
24 McGehee MD. Fast-track solar cells. Nature, 2013, 501: 323–325
25 Grätzel M. The light and shade of perovskite solar cells. Nat Mater, 2014, 13: 838–842
26 Hahn H, Mutschke U. Untersuchungen über ternäre chalkogenide. XI. Versuche zur darstellung von thioperowskiten. Z Anorg Allg

 © Science China Press and Springer-Verlag GmbH Germany, part of Springer Nature 2021

Chem, 1957, 288: 269–278
27 Ishii M, Saeki M, Sekita M. Vibrational spectra of barium-zirconium sulfides. Mater Res Bull, 1993, 28: 493–500
28 Bennett JW, Grinberg I, Rappe AM. Effect of substituting of S for O: The sulfide perovskite $BaZrS_3$ investigated with density functional theory. Phys Rev B, 2009, 79: 235115
29 Brehm JA, Bennett JW, Schoenberg MR, *et al.* The structural diversity of ABS_3 compounds with d^0 electronic configuration for the B-cation. J Chem Phys, 2014, 140: 224703
30 Sun YY, Agiorgousis ML, Zhang P, *et al.* Chalcogenide perovskites for photovoltaics. Nano Lett, 2015, 15: 581–585
31 Meng W, Saparov B, Hong F, *et al.* Alloying and defect control within chalcogenide perovskites for optimized photovoltaic application. Chem Mater, 2016, 28: 821–829
32 Ju MG, Dai J, Ma L, *et al.* Perovskite chalcogenides with optimal bandgap and desired optical absorption for photovoltaic devices. Adv Energy Mater, 2017, 7: 1700216
33 Perera S, Hui H, Zhao C, *et al.* Chalcogenide perovskites—An emerging class of ionic semiconductors. Nano Energy, 2016, 22: 129–135
34 Niu S, Huyan H, Liu Y, *et al.* Bandgap control *via* structural and chemical tuning of transition metal perovskite chalcogenides. Adv Mater, 2017, 29: 1604733
35 Gross N, Sun YY, Perera S, *et al.* Stability and band-gap tuning of the chalcogenide perovskite $BaZrS_3$ in Raman and optical investigations at high pressures. Phys Rev Appl, 2017, 8: 044014
36 Wei X, Hui H, Perera S, *et al.* Ti-alloying of $BaZrS_3$ chalcogenide perovskite for photovoltaics. ACS Omega, 2020, 5: 18579–18583
37 Wei X, Hui H, Zhao C, *et al.* Realization of $BaZrS_3$ chalcogenide perovskite thin films for optoelectronics. Nano Energy, 2020, 68: 104317
38 Comparotto C, Davydova A, Ericson T, *et al.* Chalcogenide perovskite $BaZrS_3$: Thin film growth by sputtering and rapid thermal processing. ACS Appl Energy Mater, 2020, 3: 2762–2770
39 Gupta T, Ghoshal D, Yoshimura A, *et al.* An environmentally stable and lead-free chalcogenide perovskite. Adv Funct Mater, 2020, 30: 2001387
40 Yu Z, Wei X, Zheng Y, *et al.* Chalcogenide perovskite $BaZrS_3$ thin-film electronic and optoelectronic devices by low temperature processing. Nano Energy, 2021, 85: 105959
41 Hanzawa K, Iimura S, Hiramatsu H, *et al.* Material design of green-light-emitting semiconductors: Perovskite-type sulfide $SrHfS_3$. J Am Chem Soc, 2019, 141: 5343–5349
42 Zhang H, Ming C, Yang K, *et al.* Chalcogenide perovskite $YScS_3$ as a potential p-type transparent conducting material. Chin Phys Lett, 2020, 37: 097201
43 Yin WJ, Shi T, Yan Y. Unusual defect physics in $CH_3NH_3PbI_3$ perovskite solar cell absorber. Appl Phys Lett, 2014, 104: 063903
44 Yin WJ, Shi T, Yan Y. Unique properties of halide perovskites as possible origins of the superior solar cell performance. Adv Mater, 2014, 26: 4653–4658
45 Agiorgousis ML, Sun YY, Zeng H, *et al.* Strong covalency-induced recombination centers in perovskite solar cell material $CH_3NH_3PbI_3$. J Am Chem Soc, 2014, 136: 14570–14575
46 Brandt RE, Stevanović V, Ginley DS, *et al.* Identifying defect-tolerant semiconductors with high minority-carrier lifetimes: Beyond hybrid lead halide perovskites. MRS Commun, 2015, 5: 265–275
47 Meggiolaro D, Motti SG, Mosconi E, *et al.* Iodine chemistry determines the defect tolerance of lead-halide perovskites. Energy Environ Sci, 2018, 11: 702–713
48 Kurchin RC, Gorai P, Buonassisi T, *et al.* Structural and chemical features giving rise to defect tolerance of binary semiconductors. Chem Mater, 2018, 30: 5583–5592
49 Park JS, Kim S, Xie Z, *et al.* Point defect engineering in thin-film solar cells. Nat Rev Mater, 2018, 3: 194–210
50 Kang J, Wang LW. High defect tolerance in lead halide perovskite $CsPbBr_3$. J Phys Chem Lett, 2017, 8: 489–493
51 Kresse G, Furthmüller J. Efficiency of *ab-initio* total energy calculations for metals and semiconductors using a plane-wave basis set. Comput Mater Sci, 1996, 6: 15–50
52 Blöchl PE. Projector augmented-wave method. Phys Rev B, 1994, 50: 17953–17979
53 Kresse G, Joubert D. From ultrasoft pseudopotentials to the projector augmented-wave method. Phys Rev B, 1999, 59: 1758–1775
54 Perdew JP, Ruzsinszky A, Csonka GI, *et al.* Restoring the density-gradient expansion for exchange in solids and surfaces. Phys Rev Lett, 2008, 100: 136406
55 Dudarev SL, Botton GA, Savrasov SY, *et al.* Electron-energy-loss spectra and the structural stability of nickel oxide: An LSDA + U study. Phys Rev B, 1998, 57: 1505–1509
56 Heyd J, Scuseria GE, Ernzerhof M. Hybrid functionals based on a screened Coulomb potential. J Chem Phys, 2003, 118: 8207–8215
57 Lelieveld R, IJdo DJW. Sulphides with the $GdFeO_3$ structure. Acta Crystlogr B Struct Sci, 1980, 36: 2223–2226
58 Zhang SB, Northrup JE. Chemical potential dependence of defect formation energies in GaAs: Application to Ga self-diffusion. Phys Rev Lett, 1991, 67: 2339–2342
59 Freysoldt C, Grabowski B, Hickel T, *et al.* First-principles calculations for point defects in solids. Rev Mod Phys, 2014, 86: 253–305
60 Miyake T, Aryasetiawan F, Imada M. *Ab initio* procedure for constructing effective models of correlated materials with entangled band structure. Phys Rev B, 2009, 80: 155134
61 Shih BC, Abtew TA, Yuan X, *et al.* Screened Coulomb interactions of localized electrons in transition metals and transition-metal oxides. Phys Rev B, 2012, 86: 165124
62 Shih BC, Zhang Y, Zhang W, *et al.* Screened Coulomb interaction of localized electrons in solids from first principles. Phys Rev B, 2012, 85: 045132
63 Liu C, Yang Y, Xia X, *et al.* Soft template-controlled growth of high-quality $CsPbI_3$ films for efficient and stable solar cells. Adv Energy Mater, 2020, 10: 1903751
64 Mostofi AA, Yates JR, Lee YS, *et al.* Wannier90: A tool for obtaining maximally-localised Wannier functions. Comput Phys Commun, 2008, 178: 685–699
65 Deslippe J, Samsonidze G, Strubbe DA, *et al.* BerkeleyGW: A massively parallel computer package for the calculation of the quasiparticle and optical properties of materials and nanostructures. Comput Phys Commun, 2012, 183: 1269–1289
66 Leslie M, Gillan NJ. The energy and elastic dipole tensor of defects in ionic crystals calculated by the supercell method. J Phys C-Solid State Phys, 1985, 18: 973–982
67 Heyd J, Peralta JE, Scuseria GE, *et al.* Energy band gaps and lattice parameters evaluated with the Heyd-Scuseria-Ernzerhof screened hybrid functional. J Chem Phys, 2005, 123: 174101
68 Bang J, Sun YY, Abtew TA, *et al.* Difficulty in predicting shallow defects with hybrid functionals: Implication of the long-range exchange interaction. Phys Rev B, 2013, 88: 035134

Acknowledgements This work was supported by the National Natural Science Foundation of China (11774365), the Natural Science Founda-

 © Science China Press and Springer-Verlag GmbH Germany, part of Springer Nature 2021

tion of Shanghai (19ZR1421800), Shanghai International Cooperation Project (20520760900), the Opening Project and Science Foundation for Youth Scholar of State Key Laboratory of High Performance Ceramics and Superfine Microstructures (SKL201804 and SKL201803SIC). Zeng H thanks the support by US National Science Foundation (NSF) (CBET-1510121) and US Department of Energy (DOE) (DEEE0007364). Zhang S thanks the support by US NSF (CBET-1510948). Zhang P thanks the support by US NSF (DMR-1506669). Gao W thanks the support by the Fundamental Research Funds for the Central Universities (DUT21RC(3)033) and the computational resources provided by NERSC of the US DOE (DEAC02-05CH11231), the Texas Advanced Computing Center (TACC) and Shanghai Supercomputer Center.

Author contributions Sun YY initiated and coordinated the research. Wu X, Chai J and Ming C conducted the defect calculations. Gao W and Zhang P conducted the RPA calculations. Chen M, Zeng H and Zhang S participated in the analysis of the results. Sun YY, Wu X, Gao W, Ming C, Zeng H, Zhang P and Zhang S wrote the paper.

Conflict of interest The authors declare that they have no conflict of interest.

Supplementary information Supporting data are available in the online version of the paper.

Xiaowei Wu received her BSc degree from the School of Physics and Electronic Information Engineering, Neijiang Normal University in 2016, and her Master degree from the School of Resources, Environment and Materials, Guangxi University in 2020. She joined the State Key Laboratory of High Performance Ceramics and Superfine Microstructure, Shanghai Institute of Ceramics, Chinese Academy of Sciences in 2020 as a research assistant. Her current research focuses on the defect properties in energy materials using first-principles calculations.

Weiwei Gao is currently an associate professor at the School of Physics, Dalian University of Technology. He received his PhD degree from the Department of Physics, The State University of New York at Buffalo and did postdoctoral research at Oden Institute for Computational Engineering and Sciences, University of Texas at Austin. His research interests focus on developing new methods for efficient excited-states calculations and applying computational approach on studying novel materials.

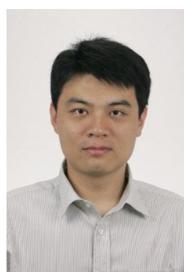

Chen Ming received his PhD degree from Fudan University in 2012. He joined the State Key Laboratory of High Performance Ceramics and Superfine Microstructure, Shanghai Institute of Ceramics, Chinese Academy of Sciences in 2014 as a postdoc and then as a research associate. His research interests are theoretical explorations of novel materials for optoelectronics and energy applications.

Yi-Yang Sun received his PhD degree from the National University of Singapore (NUS) in 2004. He worked as postdoc at the NUS, National Renewable Energy Laboratory, and Rensselaer Polytechnic Institute (RPI). In 2010, he was appointed research assistant professor and later research scientist at the RPI. In 2017, he assumed a professor position at Shanghai Institute of Ceramics, Chinese Academy of Sciences. His research focuses on the study of energy-related materials using the first-principles computations.

硫族钙钛矿光伏材料$BaZrS_3$的缺陷容忍性

吴晓维[1†], 高威帷[2,3†], 柴骏[1], 明辰[1*], 陈苗根[4], 曾浩[5], 张培鸿[5], 张绳百[6], 孙宜阳[1*]

摘要 硫族钙钛矿具有比氧化物钙钛矿更低的带隙以及比卤化物钙钛矿更高的稳定性, 有望应用于光伏和光电领域. 在这类应用中, 理想的材料往往需要避免存在复合中心的深能级缺陷, 即缺陷容忍性. 本文采用密度泛函理论(DFT)研究了一种典型硫族钙钛矿材料$BaZrS_3$的本征缺陷. 我们比较了Hubbard-U和杂化泛函这两种广泛用于解决DFT中半局域泛函带隙问题的方法. 研究发现, 通过调整U值获得与实验一致的带隙, 并将该U值用于缺陷计算, 可能会导致缺陷态过度局域化. 而杂化泛函计算则可以准确得到$BaZrS_3$的带隙. 采用这两种计算方法均会形成小的S原子团簇, 这些团簇倾向于通过自钝化来避免产生带隙中的深能级. 尽管在杂化泛函计算中观察到一些能级相对较深的缺陷, 但是在热平衡条件下制备的材料中, 由于过高的形成能, 这些缺陷的作用可以被忽略. 因此, $BaZrS_3$具有足够的缺陷容忍性, 有望应用于光伏和光电领域.

 © Science China Press and Springer-Verlag GmbH Germany, part of Springer Nature 2021